Precursor concentration induced nanostructural evolution of electrodeposited ZnO thin films and its effect on their optical and photocatalytic properties

Sathi Chatterjee[1],* 🄳 and Asit Kumar Kar[1]

[1] *Micro and Nano-science Laboratory, Department of Physics, Indian Institute of Technology (Indian School of Mines), Dhanbad 826004, Jharkhand, India*

ABSTRACT

A series of ZnO thin films has been synthesized using an electrodeposition system on Indium tin oxide (ITO) coated glass substrate by varying zinc nitrate concentration. For the synthesized thin films, the composition, morphology, crystalline structure, and optical properties are characterized using Fourier transform infrared spectroscopy (FTIR), scanning electron microscopy (SEM), grazing incidence X-ray diffraction spectroscopy (GIXRD), UV–Vis absorption spectroscopy, and photoluminescence spectroscopy (PL). The formation of Zn–O bonds and the increment of nitrate and –OH groups with increasing zinc nitrate concentration are revealed by FTIR spectroscopy. The GIXRD results show a slight shift towards the higher 2θ angle for all ZnO-related diffraction peaks, confirming the presence of micro-strain in all electrodeposited thin films. The estimated strain values increase with increasing precursor concentration, justifying the increment in crystal defects. SEM images exhibit an evolution of surface morphologies from nanosphere-like to nanosheet or nanoleaf-like structures with the zinc nitrate concentration increment. UV–Vis spectra reveal a red shift in band edge absorption from the lowest to highest zinc nitrate concentration sample; however, the edge again exhibits a blue shift for the moderate zinc nitrate concentration thin film. The calculated bandgap values for all samples are lie within the range of 3·07–2·81 eV. The PL spectra declare an enhancement in emission intensity with increasing precursor concentration. This variation in emission intensity is explained by the change in nanostructures that eventually tuned the defect states and subsequently the luminescence. A UV-light-driven photocatalytic degradation of MO dye in water has been studied to assess the photocatalytic activities of ZnO thin films using UV–Vis absorption spectroscopy. The results show the best photocatalytic efficiency (70.43%) for moderate precursor concentration thin film, achieved by an optimum concentration of surface oxygen vacancy states. However, due to a huge surface oxygen vacancy, the highest precursor concentration thin film exhibits

Address correspondence to E-mail: sathi1994.17dr000342@ap.ism.ac.in

the minimum catalytic efficiency (32.36%). It declares that an excessive amount of surface oxygen vacancy can create bulk oxygen vacancies, which eventually ruins the catalytic activity and reduces the photocatalytic performance.

1 Introduction

Various textile industries produce wastewater, and it carries several organic pollutants. Among all of the organic pollutants, organic dyes are the most common ones. These dyes are very toxic in nature and often mixed with natural water; ingestion of such dyes through water is extremely harmful to human health. Therefore, it is imperative to degrade such dyes, and an appropriate way for the degradation is using any catalyst with exposure to light. Photocatalysis using semiconductor material appears to be an excellent technique because of various benefits like non-toxicity, low energy consumption, low cost, and the capability to effectively employ both visible and UV lights [1]. Due to the characteristics like higher photoefficiency and excellent electronic properties, ZnO has achieved great popularity for the degradation of organic pollutants among all other semiconductors [2].

ZnO is an n-type semiconductor having a high exciton binding energy as well as a wide bandgap of 3.37 eV [3]. It serves various applications like photodiodes [4], light-emitting diodes [5], photocatalysis [6–9], solar cells [10], gas sensors [11], etc. The ZnO nanostructured thin films are possible to synthesize using several methods: hydrothermal [12], MOCVD [13], spray pyrolysis [14], dip coating [15], spin coating [16], electrodeposition [8, 17], etc. However, among many high-temperature synthesis techniques, electrodeposition has several advantages like simplicity, low cost and power consumption, easily controllable and scalable, etc. [18]. Moreover, using the electrodeposition method, various kinds of nanostructures with attractive morphology can be grown on the substrate in the absence of any template [19, 20]. Depending on these diverse and interesting nanostructures, different properties of the thin films like optical, photocatalytic properties, etc., can be tuned. In the electrodeposition method, the ZnO thin films are deposited on various substrates, and as precursors, zinc nitrate, zinc acetate and zinc chloride are often used [21–23]. However, only a few research works have focused on the detailed analysis of the influence of precursor concentration on various properties of ZnO thin films electrodeposited on ITO/glass substrates. For instance, Yang et al. have synthesized electrodeposited ZnO thin films on ITO/glass substrate and studied the effect of zinc nitrate concentration on the growth mechanism and optical properties of the thin films [24]. Similarly, the influence of zinc chloride concentration on morphological and structural properties of ZnO thin films electrodeposited on ITO/glass substrate was studied by Dakhsi et al. [25]. They have also analyzed the kinetics of the thin films' growth with varying zinc chloride concentrations. Again, Singh et al. [26] have synthesized electrodeposited ZnO thin films at low temperatures by varying zinc nitrate concentrations and studied the influence of precursor concentration on the structural as well as optical properties of the thin films. In all these reported literature, the various properties (optical, morphological, structural) of the thin films are only examined by the variation of precursor concentration; however, there has been hardly a consideration of the correlation between the attractive crystal or morphological structures and the optical properties of the electrodeposited ZnO thin films.

So far, several reports have focused on the role of zinc nitrate concentration on the variation of morphology for electrodeposited ZnO thin films. For instance, the morphological evolution of electrodeposited ZnO thin films from 1D nanorods to 2D nanosheets has been discussed by Xue et al. just by changing zinc nitrate concentration [27]. They have found that for low zinc nitrate concentration, the growth of ZnO nanostructure becomes fast along the c-direction, leading 1D nanorod-like structure. However, as the precursor concentration increases, the growth along c-direction gets hindered due to the adsorption of NO_3^- ions on the (0001) plane, and hence, 2D nanosheet-like structure is formed. Pradhan et al. [28] have synthesized ZnO nanostructured thin films with various dimensions on ITO/glass substrate by electrodeposition method. They have successfully grown 1D nanospikes and nanopillars to 2D nanowalls and nanodisks by varying the zinc

nitrate concentration and then investigated the role of zinc nitrate concentration on controlling the dimensionality of the nanostructures. Khajavi et al. [29] have successfully synthesized 1D ZnO nanowire arrays with varying zinc nitrate concentration using the electrodeposition process. To explain the nucleation and growth of ZnO nanowires, they have proposed a model based on the concentration of OH^- ions which is produced from the reduction of NO_3^- ions and the Zn^{2+} ions. The authors have observed that, at a high concentration of zinc nitrate, the ratio of OH^- and Zn^{2+} ions becomes high and the nanowires' lateral growth is suspended. But, as the ratio of OH^- and Zn^{2+} ions decreases, the lateral growth of the nanowires is initiated due to the diffusion of Zn^{2+} ions along the nanowires. The variation in surface topography with different zinc nitrate concentrations for 1D nanorod like ZnO thin films has been studied by Yao et al., where they have witnessed a remarkable increment in homogeneity and diameter of ZnO nanorods with the increment of precursor concentration [30]. However, there is hardly any detailed investigation on the evolution of electrodeposited ZnO thin films from 3D nanosphere-like structure to 2D nano leaf-like structure just by varying zinc nitrate concentration.

On the other hand, there are many works studying the photocatalytic activity of ZnO thin films through changing zinc nitrate concentration. For instance, Zhao et al. [31] have examined the photocatalytic performance of the electrodeposited ZnO thin films synthesized by zinc nitrate concentration variation and reported higher photocatalytic performance of the samples due to the unique network-like structure made of 2D nanosheets with higher light absorption ability and higher specific surface area. Similarly, Lv et al. [32] have investigated the UV light response of the hydrothermally synthesized ZnO thin films by varying zinc nitrate concentrations. The authors have reported a much higher catalytic activity for the spherical nanoparticles due to the higher number of cracks in the surface of the thin films. Whereas, for the nanosheet-like structures, the ability of lower photocatalytic activity in polar planes than nonpolar planes results in the reduction of catalysis performances. Again, the photocatalytic degradation of MO dye using electrodeposited ZnO thin films as a catalyst is also investigated by Cataño et al. [33], and they have explained the degradation results based on the variation in specific surface areas. However, very few

works [34–36] have focused on the impact of the variation in surface oxygen vacancy concentration on the photocatalytic performances of the different nanostructured ZnO thin films, and these works have shown only enhancement in the catalysis results with the increase in surface oxygen vacancy concentration. But there is no report to date studying the harmful outcome of excessive concentration of surface oxygen vacancies on the catalytic efficiency. Also, the requirement of optimizing surface oxygen vacancy concentration to enhance photocatalytic activity is never investigated.

Therefore in this work, a series of ZnO thin films have been electrodeposited by varying the zinc nitrate precursor concentration. For the deposited thin films, a correlated study has been presented between the precursor concentration and the optical, structural, and morphological properties. Finally, the photocatalytic activity of ZnO thin films has been studied through the degradation of MO dye, and the effect of surface oxygen vacancy concentration on the activity has been investigated.

2 Experimental techniques

2.1 Materials used

Potassium chloride (KCl), Zinc nitrate hexa-hydrate [Zn $(NO_3)_2 \cdot 6H_2O$], and distilled water were bought from Sigma Aldrich. As a solvent, Distilled water was used during the experiment.

2.2 Synthesis of ZnO thin films

Zinc oxide thin films were deposited on ITO coated glass substrate by the two-electrode electrodeposition method, where two electrodes are separated by a distance of about 1 cm. At first, all the substrates were washed mechanically using soap solution, ultrasonicated in a successive bath of acetone, ethanol, and DI water for 20 min, and finally, dried in an oven at 60 °C for 1 h. All the thin films were electrodeposited with a 2.3 V potential difference and for deposition time of 20 min using a graphite rod as an anode and ITO coated glass substrates as a cathode with the area and sheet resistance of about 0.5×1 cm^2 and 10 Ω/cm^2, respectively. Aqueous solutions of zinc nitrate hexahydrate (0.0015 M, 0.0020 M, 0.0025 M) and potassium chloride (0.1 M) in 20 mL

DI water were used as electrolytes. Thus, all the thin films were synthesized by changing the molar proportion of zinc nitrate hexahydrate to KCl viz. 0.0015:0.1, 0.0020:0.1, and 0.0025:0.1; and they were named as S1, S2, and S3, respectively.

2.3 Characterizations

In order to identify different crystallite phases of ZnO thin films, GIXRD was studied using a Panalytical Xpert ultra-fast diffractometer with Cu Kα (λ = 0.154056 nm) radiation considering the Bragg–Brentano configuration between 20° and 80° (step size of 0.02° and counting time of 2 s) in θ–2θ scanning mode. SEM (FESEM supra-55) was used to characterize the shape, size, and growth of the morphological structures of the samples. The presence of different vibrational bonds was studied by using FTIR (Shimadzu Corpn, Japan, IR-Prestige 21) spectroscopy. Using UV–VIS spectroscopy (Agilent Cary 5000), the absorption spectra were taken in 200–800 nm range and the PL emission spectra (Jobin Yvon Flurolog-3–11 spectroflurimeter) were investigated in the range of 300–550 nm by using a xenon lamp with a power of 450 W and with an excitation wavelength of 285 nm.

2.4 Photocatalytic activity

The photocatalytic performance of all ZnO thin film samples is analyzed to degrade methyl orange (MO) dye solution by irradiating UV light. The catalytic experiment was performed in a photoreactor equipped with a Philip currency detection UV lamp with a power of 8 W and a radiation wavelength of 235 nm. Throughout the experiment, the distance between the beaker and the UV lamp was kept at around 10 cm, and the light was irradiated perpendicular to the suspension surface of the beaker containing the MO dye solution. Initially, a dye solution of 100 mL (concentration of 10 mg/L) was prepared through stirring for 20 min. Furthermore, to achieve adsorption–desorption equilibrium, the thin films were dipped in the dye solution and stirred in the dark for about 30 min before illumination. Then, the UV light source was kept on for 6 h, and in every 1 h interval, about 5 mL of solution was taken from the suspension using a dropper. Finally, to realize the catalytic activity, the catalyst-MO dye solution collect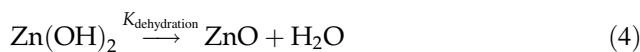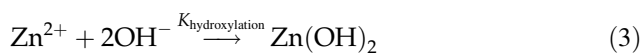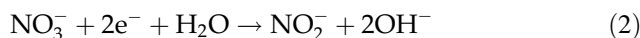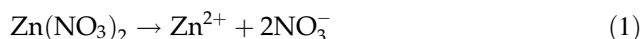ed every 1 h was characterized by using a UV–Vis spectrophotometer in the range of 200 − 800 nm and the suppression of the MO dye absorption peak centered at 465 nm was measured. The entire photocatalytic experiment was conducted at room temperature.

3 Results and discussion

### 3.1 Morphology and growth mechanism of electrodeposited ZnO thin films

Morphologies of all ZnO thin films deposited on ITO coated glass substrate are given in Fig. 1a, b, and c. Both samples S1 and S2 show a nanosphere-like structure, while sample S3 exhibits a nanosheet or leaf-like structure. The average particle size for every sample is estimated using the Image J software. For S1 and S2, the average particle size is 71.6 nm and 150.4 nm, respectively. Again, for S3, the nanosheet-like structure's average length and width are respectively 350.8 nm and 43.2 nm.

The different nanostructures are deposited on ITO-coated glass substrate via the following reactions [31]

$$Zn(NO_3)_2 \rightarrow Zn^{2+} + 2NO_3^- \tag{1}$$

$$NO_3^- + 2e^- + H_2O \rightarrow NO_2^- + 2OH^- \tag{2}$$

$$Zn^{2+} + 2OH^- \xrightarrow{K_{\text{hydroxylation}}} Zn(OH)_2 \tag{3}$$

$$Zn(OH)_2 \xrightarrow{K_{\text{dehydration}}} ZnO + H_2O \tag{4}$$

At first, when the potential was applied, zinc nitrate was immediately broken down into Zn^{2+} cations and NO_3^- anions. Afterward, the mass transfer in liquid phase occurs by the migration of produced NO_3^- anions to the liquid layer near the cathode surface. Then, at step (2) of the reaction, these NO_3^- anions are reduced by utilizing electrons to form nitrite ions (NO_2^-) and also generate OH^- ions for the formation of ZnO. Further, when an adequate amount of hydroxyl ion is present, the solution reaches its supersaturation state and $Zn(OH)_2$ is formed by the hydroxylation process. Finally, $Zn(OH)_2$ is dehydrated and generates ZnO nuclei. Then, by the heterogeneous nucleation process, these ZnO nuclei form ZnO nanoclusters which eventually develop ZnO nanocrystallites. In the case of the low zinc nitrate concentration sample (S1), the dehydration rate is greater than the rate of hydroxylation, i.e., $K_{\text{dehydration}} > K_{\text{hydroxylation}}$ [31]. That

Fig. 1 **a**, **b** and **c** SEM images (2 × 2 μm) of S1, S2, and S3, respectively
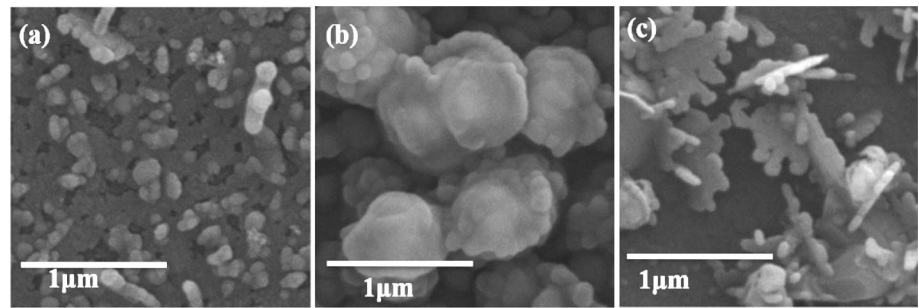
means, for the low precursor concentration sample, the production of ZnO nuclei is faster than the generation of $Zn(OH)_2$ moieties. So, the ZnO nanocrystals in S1 grow uniformly without any hindrance, showing a nanosphere-like structure. But, when the zinc nitrate concentration becomes a little higher (i.e., for S2), the degree of supersaturation of the electrolyte solution exceeds its critical value, and hence the size of ZnO nanoclusters increases by attaching new ZnO nanoclusters to the exciting nanoclusters' surface. Hence, agglomerated ZnO nanosphere-like structure is formed. The schematic diagram of the complete illustration of nanosphere and agglomerated nanosphere-like structure is given in Fig. 2. Furthermore, in the case of S3, as the concentration of zinc nitrate is high, so the rate of hydroxylation process is higher than the rate of the dehydration process, i.e., $K_{hydroxylation} > K_{dehydration}$ [37]. Because, when the concentration of zinc nitrate becomes high, the concentration of Zn^{2+} ions increases automatically, enhancing the rate of the hydroxylation process. Thus, due to the relatively faster hydroxylation process, the dehydration of $Zn(OH)_2$ gets delayed. That means, for the high precursor concentration, the

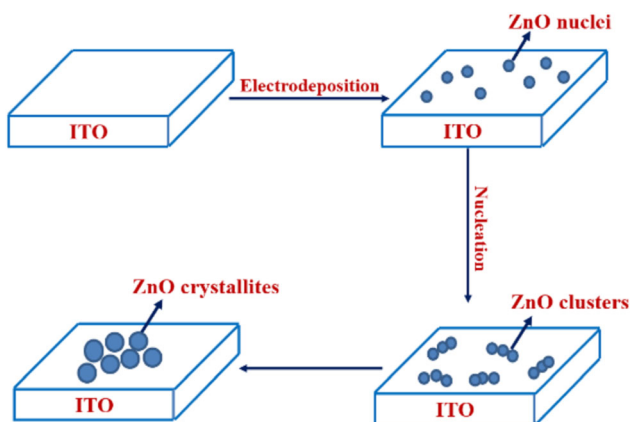generation of $Zn(OH)_2$ is faster than the formation of ZnO, and it suggests the termination of growth of ZnO along [0001] direction. The schematic diagram of the nanosheet or nanoleaf-like structure is given in Fig. 3. For ZnO, the polar plane (0001) has the fastest growth among all planes. This polar plane has two faces; one is Zn^{2+} terminated polar plane (0001) and another is the O^{2-} terminated polar plane $(000\bar{1})$. Hence ZnO has a net dipole moment along the vertical axis (i.e., *c*-axis). In the case of S3, as the zinc nitrate concentration is high, more OH^- ions are produced, and due to electrostatic force, these OH^- ions are attracted to the Zn^{2+} terminated surface.

Finally, these ions act as a capping agent inhibiting further adsorption of more OH^- ions on the polar plane (Zn^{2+} terminated surface), and consequently, the crystal growth along the vertical axis gets suppressed. Therefore, the crystal grows favorably towards the non-polar plane $(10\bar{1}0)$ and results in the formation of 2D nanosheet or nanoleaf-like structure.
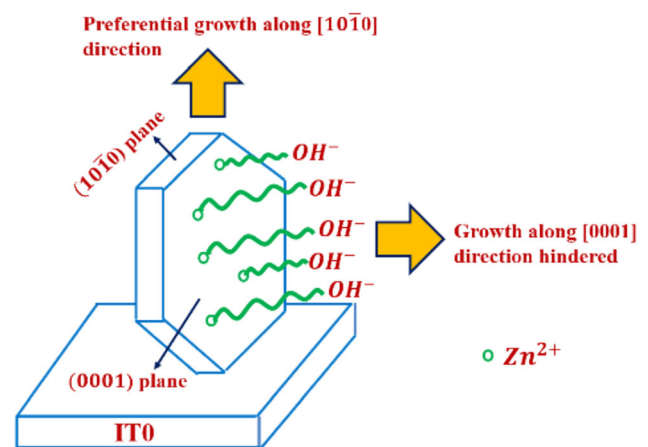

Fig. 2 Schematic illustration of the formation of ZnO nanosphere thin film

Fig. 3 Schematic diagram of nanosheet formation

3.2 Structural analysis

3.2.1 GIXRD analysis

The GIXRD spectra of electrodeposited ZnO thin films are provided in Fig. 4. For all samples, the corresponding spectra showed peaks at 30.45°, 35.43°, 37.49°, 40°, 45°, 50.85°, 60.67°, and 66°. Among these, a few are matched with ITO, and others are of the hexagonal wurtzite structure of ZnO. The peaks at 30.45°, 40°, 50.85°, and 60.67° are well-matched with the JCPDS file No. 01-089-4596 of ITO [38]. On the other hand, the peaks at 35.43°, 37.49°, 45°, and 66° correspond to the lattice planes (002), (101), (102), and (112) of ZnO, respectively.

However, the peaks related to ZnO do not exhibit an exact match with the standard JCDPS file 00–036-1451; instead, they are slightly shifted (− 1°) towards the higher 2θ. The reason for shifting in the peak positions may be relevant to the appearance of micro-strain in the samples [39].

From the GIXRD spectra of S1 and S2, it is observed that the peaks corresponding to (002) and (101) planes show an enhancement in intensity, indicating various degrees of orientation and growth in these directions and recompensing various distances from a hexagon's center to its edges which leads to the creation of nanosphere like structure. For S2, a new peak corresponding to the plane (112) is observed, and the intensity of all the ZnO-related diffraction
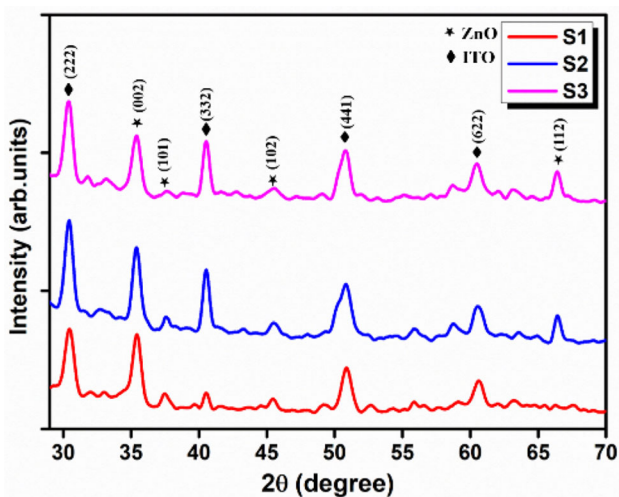

Fig. 4 GIXRD patterns of ZnO thin films S1, S2, and S3 electrodeposited on ITO/glass substrates with increasing precursor concentration in the electrolyte where all the films possess wurtzite crystal structure

peaks along with (002) and (101) are higher compared to S1, which suggests a higher crystallinity for S2 than S1. But, in the case of S3, the intensity of (002) peak is lower than S1 and S2, and the intensity of other ZnO-related diffraction peaks are also low, which signifies a lower crystallinity of S3 compared to S1 and S2. The suppression of peak (002) for the sample S3 indicates that the growth along [0001] direction has decreased and the growth along nonpolar planes has increased. This suppression of preferential growth along the c-axis gives the nanosheet or nanoleaf-like structure for S3. Furthermore, to gain more knowledge about the preferential growth and orientation of each thin film, the degree of orientation along the most intense peak (002) is evaluated by the relation

$$P = \frac{I_{002}}{\sum I(\text{hkl})} \qquad (5)$$

where I_{002} is the intensity of diffraction peaks along the (002) plane and $\sum I(\text{hkl})$ is the sum of the intensities of all ZnO-related diffraction peaks. For S1, S2, and S3 samples, the estimated values of P are 0.45, 0.51, and 0.42, respectively. The ratio values reflect an increment from S1 to S2 and then a decrement for S3. The increment in intensity ratio from S1 to S2 implies the increase of growth along the c-axis, while the further reduction in the intensity ratio for S3 reveals the suppression of growth along the [0001] direction. This variation in intensity ratio for all thin films essentially establishes a direct connection between the XRD patterns and the observed nanostructure of all samples.

3.2.1.1 Crystallite size and strain
For ZnO thin films, the GIXRD patterns show slight shifting and broadening of diffraction peaks which may occur because of the variation in crystallite size and the presence of micro-strain [40]. The corresponding crystallite size and strain values are evaluated via the equation of William–Hall (W–H) plot which is given by [41]

$$\beta\cos\theta = \frac{\kappa\lambda}{D} + 4\varepsilon\sin\theta \qquad (6)$$

From the above Eq. (6), the term '$\beta\cos\theta$' is plotted with '$4\sin\theta$' for all ZnO thin films, and they are presented in Fig. 5. In the Figure, the values of R^2 are inserted and they are 0.402, 0.404, and 0.425 for S1, S2, and S3, respectively. For every sample, the value of R^2 is below 0.5, which designates a weak fit between the experimental data points and fitted data points.
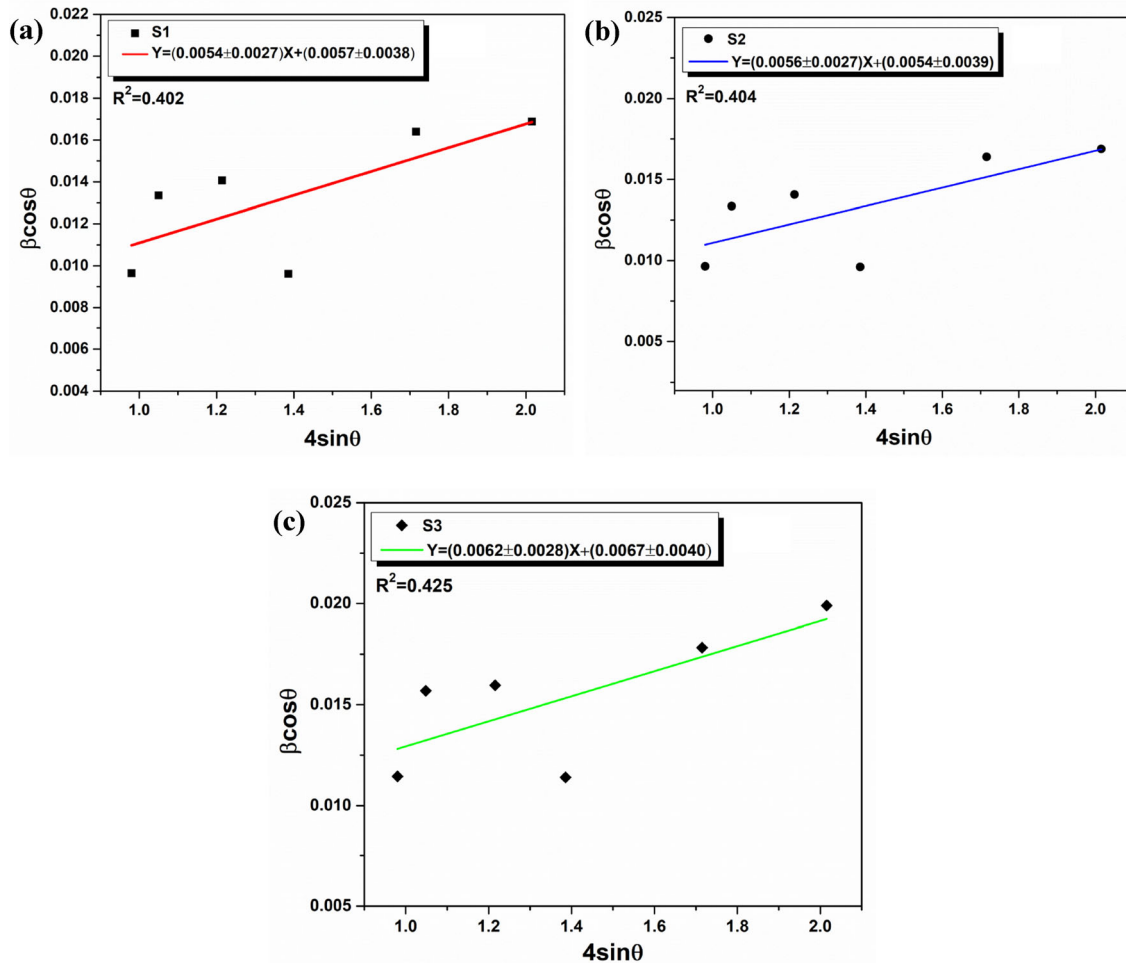
Fig. 5 W–H plot of ZnO thin films **a** S1, **b** S2 and **c** S3 electrodeposited on ITO/glass substrates with increasing precursor concentration in the electrolyte

Further, these low values of R^2 suggest a large deviation in the experimental dots for all the thin film samples, and it designates that some (hkl) planes deviate stronger compared to others, referring to the anisotropic nature of the crystal. The crystallite size and strain values for all samples are estimated from the y-intersect and the slope of the fitted line, respectively; they are listed in Table 1. The crystallite size varies within the range of (20.6 ± 9) nm to

Table 1 Crystallite Size and strain of all ZnO thin films

Sample name	Crystallite size (nm)	Strain ($\times 10^{-3}$)
S1	24.4 ± 13	5.4 ± 2.7
S2	25.6 ± 14	5.6 ± 2.7
S3	20.6 ± 9	6.2 ± 2.8

(25.6 ± 14.0) nm, and the strain ranges from $(5.4 \pm 2.7) \times 10^{-3}$ to $(6.2 \pm 2.8) \times 10^{-3}$. It is observed that with increasing the concentration of zinc nitrate, the strain value increases, leading to an increment of imperfection or defects in the crystal.

3.3 Compositional analysis

3.3.1 FTIR spectroscopy

In order to identify the existence of various expected vibrational bonds as well as the undesired bonds, FTIR spectroscopy was carried out. The FTIR spectrum of S1 (Fig. 6, inset) exhibits a strong band centered at 761 cm^{-1} assigned to the stretching vibration of Zn–O [42]. For S1, two other bands are observed at a wavenumber of 895–1647 cm^{-1} corresponding to the presence of nitrate group and bending vibration
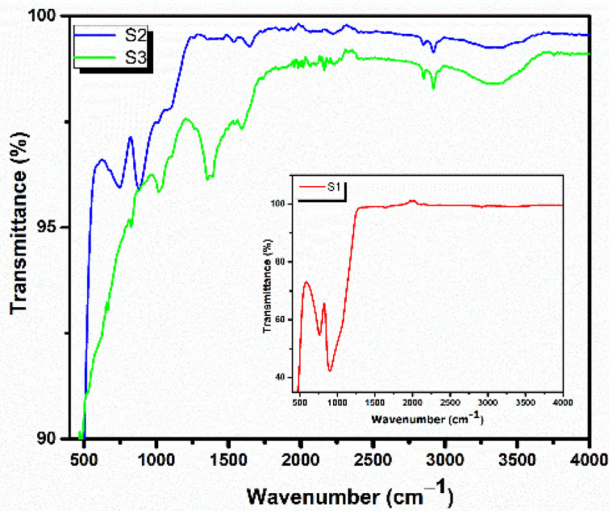
Fig. 6 FTIR spectra of ZnO thin films S1, S2 and S3 electrodeposited on ITO/glass substrates with increasing precursor concentration in the electrolyte

of –OH group, respectively [43, 44]. The FTIR spectrum for S2 shows the stretching vibrations of Zn–O bond at a wavenumber of 749 cm^{-1}. There are few bands at 880, 1544.3 and 1651.3 cm^{-1} observed for S2, which attributed to the presence of nitrate groups and bending vibration of –OH group. Again for S2, a new strong band is observed at 3339.4 cm^{-1} that is associated with the stretching vibration of –OH group on the surface of ZnO [45]. The FTIR spectrum of S3 exhibits a new weak peak corresponding to the stretching vibration of Zn–O bond at 669 cm^{-1}. For S3, the wavenumber peak related to the presence of nitrate group is centered at 880.7 cm^{-1}, and the peaks related to bending vibration of –OH group are observed at 1547.7–1591 cm^{-1}. There are two other strong bands observed at 1370–3339.4 cm^{-1}, which are attributed to the NO_3^- bending vibration [44] and the stretching vibration of –OH group on the surface of ZnO, respectively. The FTIR spectra reveal that with the increment of zinc nitrate concentration, the transmittance percentage related to the NO_3^- bending vibrational frequency becomes low. On the other hand, the spectra also imply a lower transmittance percentage value related to –OH stretching and bending vibrational bands with the increment of zinc nitrate concentration, which indicates an increase in the population of –OH groups. Furthermore, the reaction mechanism for the preparation of ZnO thin films using zinc nitrate solution shows that the presence of nitrate groups is increased with the

increment of zinc nitrate concentration. Hence the number of –OH groups increases automatically. Therefore, the increment in the population of nitrates and –OH groups with zinc nitrate concentration are consistent with the sample preparation.

3.4 Optical properties

3.4.1 UV–Vis spectroscopy

For the electrodeposited nanostructured ZnO thin films, the optical properties are analyzed by obtaining the absorption spectra. All the UV–Vis absorption spectra are given in Fig. 7a. The absorption spectra of S1 exhibit a band edge absorption at 338 nm, whereas the same for the S2 sample exists at 340 nm. Moreover, for the S3 sample, the band edge exists again at a wavelength of 335 nm. That means, with the increment of crystallite size from S1 to S2, the band edge shows a redshift, probably indicating the reduction of bandgap and consequently an increment in crystallinity. Furthermore, for S3, the band edge exhibits a blue shift compared to S1 and S2, which is related to the reduced crystallite size and a decrease in crystallinity. Again, as the crystallite size increases from S1 to S2, the grain size also increases and declares a decrement in diffuse scattering, which eventually implies a reduction in optical transparency. However, as the crystallite size reduces for S3, the grain size also decreased, suggesting an increment in optical transparency compared to S1 and S2.

The bandgap values for all ZnO thin films are determined using the relation [46]

$$\alpha(v)hv = A(hv - E_g)^{1/2} \tag{7}$$

where hv, E_g and A are the incident photon energy, optical bandgap and an arbitrary constant, respectively.

The obtained band gap values from the Tauc plot (Fig. 7b) show that with the increment of zinc nitrate concentration from 0.0015 M (S1) to 0.0020 M (S2), the bandgap value decreases from 3.04 to 2.81 eV. But for the highest precursor concentration (0.0025 M, S3), the bandgap value again increases to 3.07 eV.

In order to gain further insight on absorbance of every sample, the absorption efficiency is calculated by the following equation [47]
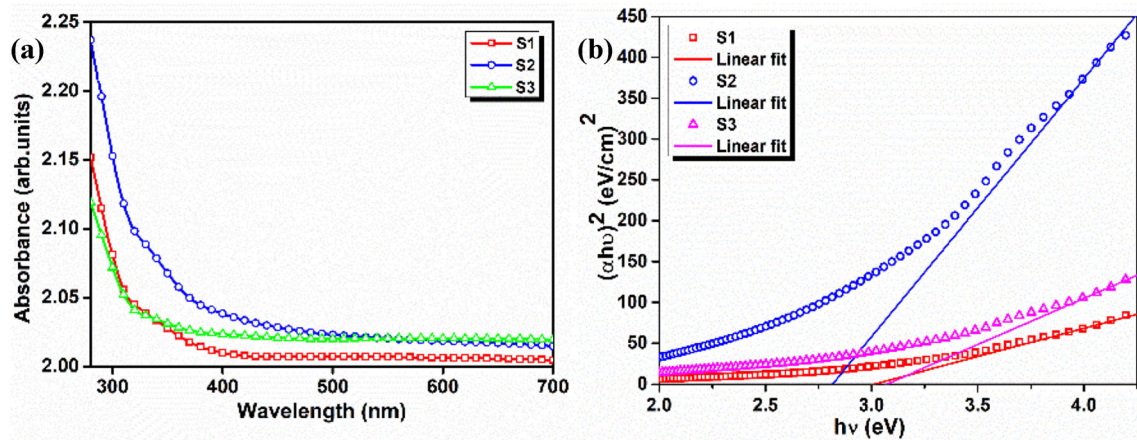
Fig. 7 a Absorption spectra and **b** Tauc plot of ZnO thin films S1, S2 and S3 electrodeposited on ITO/glass substrates with increasing precursor concentration in the electrolyte

$$\varepsilon_{abs} = N\left(\frac{\pi D^2}{4}\right)Q_{abs} \qquad (8)$$

where ε_{abs} is the extinction coefficient, D is the diameter of the particle, N is the number concentration of particles, and Q_{abs} is the absorption efficiency. The determined absorption efficiency values for S1, S2, and S3 samples are 0.28, 0.24, and 0.57 respectively. The efficiency values indicate that the sample S2 with the largest particle size and lowest bandgap shows the minimum absorption efficiency, whereas S3 with the smallest particle size and highest bandgap exhibits maximum absorption efficiency.

3.4.2 Photoluminescence spectroscopy

For all ZnO thin films, the photoluminescence spectra were recorded with a 285 nm excitation wavelength and presented in Fig. 8. It can be observed that the emission intensity increases with the increment of the concentration of zinc nitrate, i.e., from S1 to S3. The spectra reveal few UV emission peaks at 335, 350, and 395 nm (3.7, 3.54, and 3.1 eV, respectively) as well as some visible emissions peaks at 450, 467, 483, and 533 nm (2.7, 2.65, 2.56, and 2.32 eV, respectively). The emission peak at 335 nm corresponds to the excitonic band edge emission. The other two UV emission peaks at 350–395 nm arise due to inter-band transition between valance band and conduction band.

Furthermore, the visible emission peaks for ZnO thin films appeared for the presence of native point defects. There are mainly six types of native defects: zinc vacancy (V_{Zn}), oxygen vacancy (V_0), zinc interstitial (Zn_i), oxygen interstitial (O_i), oxygen anti-site
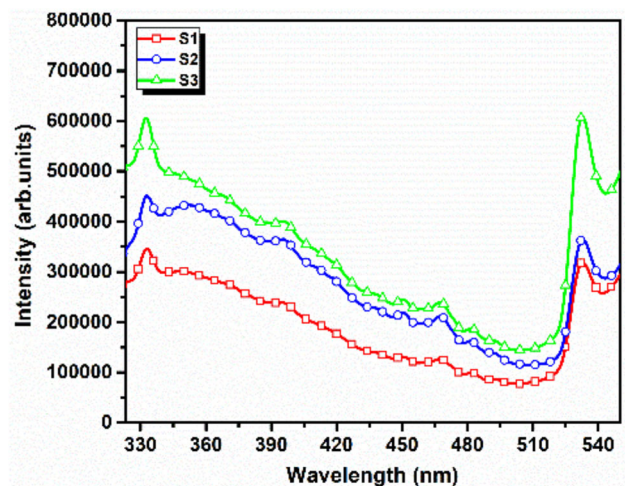

Fig. 8 Photoluminescence spectra of ZnO thin films S1, S2 and S3 electrodeposited on ITO/glass substrates with increasing precursor concentration in the electrolyte

(O_{Zn}), and zinc anti-site (Zn_0). The photoluminescence spectra of all ZnO thin films show some sharp peaks and few broad peaks. Various research suggested that the broadness of the peaks is observed as a consequence of overlapping of more than one trap level emissions.

Based on the photoluminescence spectra of all the thin films, the possible energy level diagram is given in Fig. 9. The violet emission peak at 450 nm is originated due to the transition from Zn_i to V.B. [48]. The blue emission peak centered at 467 nm emerged due to transition from C.B. to V_{Zn}, while the blue-green emission peak at 483 nm appeared via the transition from Zn_i to V_{Zn} [49, 50]. Finally, the
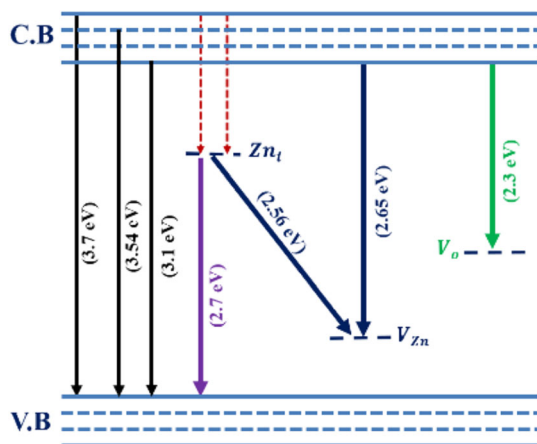
Fig. 9 Energy level diagram based on the photoluminescence spectra of ZnO thin films S1, S2 and S3 electrodeposited on ITO/glass substrates with increasing precursor concentration in the electrolyte

transition from C.B. to V_0 generates the green emission peak centered at 533 nm [51].

3.4.2.1 Role of nanostructure in defect emission In the luminescence profile of ZnO thin films, the defect states in a crystal always play a vital role. The change in photoluminescence spectra according to the variation of nanostructures (tuned by the concentration of precursor) gives a clear hint about the role of nanostructures in inducing photoluminescence spectra for the ZnO thin films. In general, the shape of each of the nanostructures decides the surface area. So, during the synthesis of ZnO thin films, there is a chance of the development of defect states either by the impurity attached to the intrinsic sites or the surface. Therefore, nanostructures really tune the defect states and necessarily cause photoluminescence in ZnO thin films.

From the schematic diagram of nanosheet or nanoleaf-like structure (Fig. 1c), it is evident that among all nanostructures, S3 has a very large polar exposed surface. So, due to having a larger polar exposed surface, the occurrence of adsorption of impurity also has a high possibility. The OH$^-$ ions (residual ions) will get attached at the available sites on the surface of the nanostructures, leading to the generation of surface defect states. Thus, due to having a huge amount of surface defect states as well as intrinsic defect levels, the luminescence intensity gets enhanced. That means, as the S3 sample has a very large exposed polar surface (0001), so more OH$^-$ ions will get attached and create surface defect states.

As a result, the emission intensity enhances and shows maximum intensity.

On the other hand, for S1 and S2, the nanostructure is spherical and agglomerated spherical nanostructure. In the case of the spherical nanostructure, the crystal growth is not favorable along a particular direction; moreover, the crystal growth occurs equally in different directions. Again, for the agglomerated spherical nanostructure, as a result of agglomeration, a tiny portion of the exposed polar surface is available in comparison with nanosheet ZnO thin film. Therefore, due to having a less exposed polar surface (0001), the availability of active sites on the surface for the adsorption of residual ions (OH$^-$) is reduced. As a result, a significantly smaller number of OH$^-$ ions is attached to the active sites present on the surface of the spherical and agglomerated spherical nanostructures, and the creation of oxygen vacancy-related surface defects states becomes automatically low. In addition, the generation of other surface defect states like Zn_i and V_{Zn} also becomes less due to a lack of exposed polar surface. This implies that the concentrations of surface defect states (i.e., V_0, Zn_i, and V_{Zn}) are decreased, suggesting a quenching in overall visible emission intensity for the nanosphere and agglomerated nanosphere-like structures compared to the nanosheet ZnO thin film. Above discussion essentially reflects that the photoluminescence spectra of ZnO thin films are controlled by both the defect states as well as nanostructures.

3.4.2.2 CIE chromaticity Based on the photoluminescence spectra (refer to Fig. 8), the chromaticity diagram of electrodeposited ZnO thin film samples is exhibited in Fig. 10. The color emitted from the thin films and the (X, Y) coordinates are determined using the chromaticity color calculator.

The calculated (X, Y) values for each sample are given in Table 2. These computed data of coordinates indicate that for the lowest zinc nitrate concentration sample, the emitted color lies in the greenish-blue region. But with the increase of precursor concentration, the color shifted towards the blue region.

Furthermore, for the higher precursor concentration sample, the emitted color shifted to the previous greenish-blue region. Therefore, it can be said that tuning of color is possible in ZnO thin films by changing the precursor concentration.
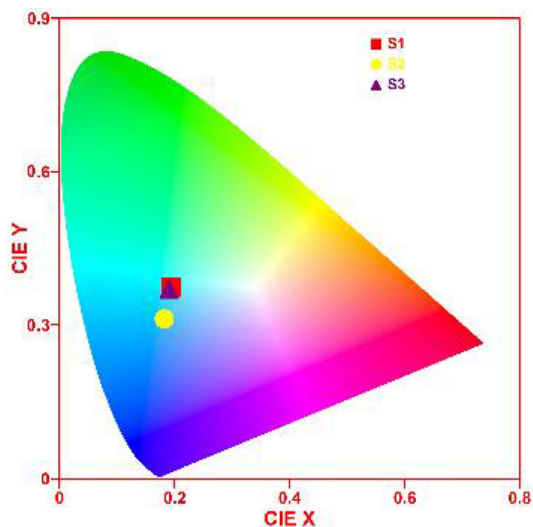
Fig. 10 CIE diagram of electrodeposited ZnO thin films

Table 2 Color coordinates and color purity of electrodeposited ZnO thin films

Sample name	X	Y
S1	0.194	0.373
S2	0.182	0.312
S3	0.191	0.367

3.5 Photocatalytic activity

Figure 11a–d exhibits the absorption spectra of MO dye solution in the presence and absence of ZnO thin film samples. The distinctive peak of MO dye at 465 nm has been observed by varying the UV exposure time. Furthermore, for understanding the catalytic performance of thin films, the degradation efficiency is determined by the following relation [52]

$$\eta = \frac{C_o - C_t}{C_o} \times 100\% \qquad (9)$$

where η defines the degradation efficiency, C_o defines the MO dye's initial concentration, and C_t represents the MO dye solution's concentration after specific UV exposure time t.

Here, the photocatalytic degradation of MO dye in the absence of any catalyst is conducted for a better comparison of the catalytic activity of the ZnO thin films. The degradation of MO dye solution in the absence and presence of ZnO catalysts is exhibited in Fig. 12. The corresponding photodegradation efficiency is determined using the relation (9) and it turned out to be 12.3%. Later, the photocatalytic degradation efficiencies of the dye solution with S1, S2, and S3 samples are calculated; they are listed in

Table 3. The efficiency values are found to be 60%, 70.43%, and 32.36% for S1, S2, and S3, respectively. From the efficiency values, it can be understood that the photocatalytic degradation is minimal in the absence of any catalyst, but the efficiency gets enhanced after the addition of catalyst.

This concludes that the photodegradation of the dye solution occurs due to the catalytic effect of ZnO thin films where no photolysis of MO dye is involved. Further, the degradation efficiency results imply that the S2 sample has the highest catalytic activity among all ZnO thin films with an efficiency order S2 > S1 > S3. In general, the photocatalytic activity of ZnO thin films depends on several factors and particle size is an important one among them. Again, the catalysis results also depend on the absorption efficiency values estimated from the absorbance results and particle size for all samples. Generally, the catalyst with smaller particle size and higher absorption efficiency shows higher catalytic activity, but the degradation results do not follow this trend for the ZnO thin films. However, other than particle size and absorption efficiency, the oxygen vacancy concentration also plays a vital role in tuning the catalytic efficiency. And, the catalysis results of the ZnO thin films can be explained by the effect of the oxygen vacancy site's concentration.

3.5.1 Kinetic modeling of the photocatalytic degradation method

In order to access more knowledge about the photocatalysis process, four kinds of kinetic models, including zero-order model (Eq. 10) [53], first-order model (Eq. 11) [54], second-order model (Eq. 12) [55], and modified Freundlich model (Eq. 13) [56], are employed.

The corresponding equations of the mentioned models are as follows

$$C_t - C_0 = Kt \qquad (10)$$

$$\ln\left(C_0/C_t\right) = Kt \qquad (11)$$

$$\left(\frac{1}{C_t} - \frac{1}{C_0}\right) = Kt \qquad (12)$$

$$\ln\left(1 - C_t/C_0\right) = \ln K + b\ln t \qquad (13)$$

where b is a constant and K is the corresponding rate constant. The experimental kinetic data fitted with
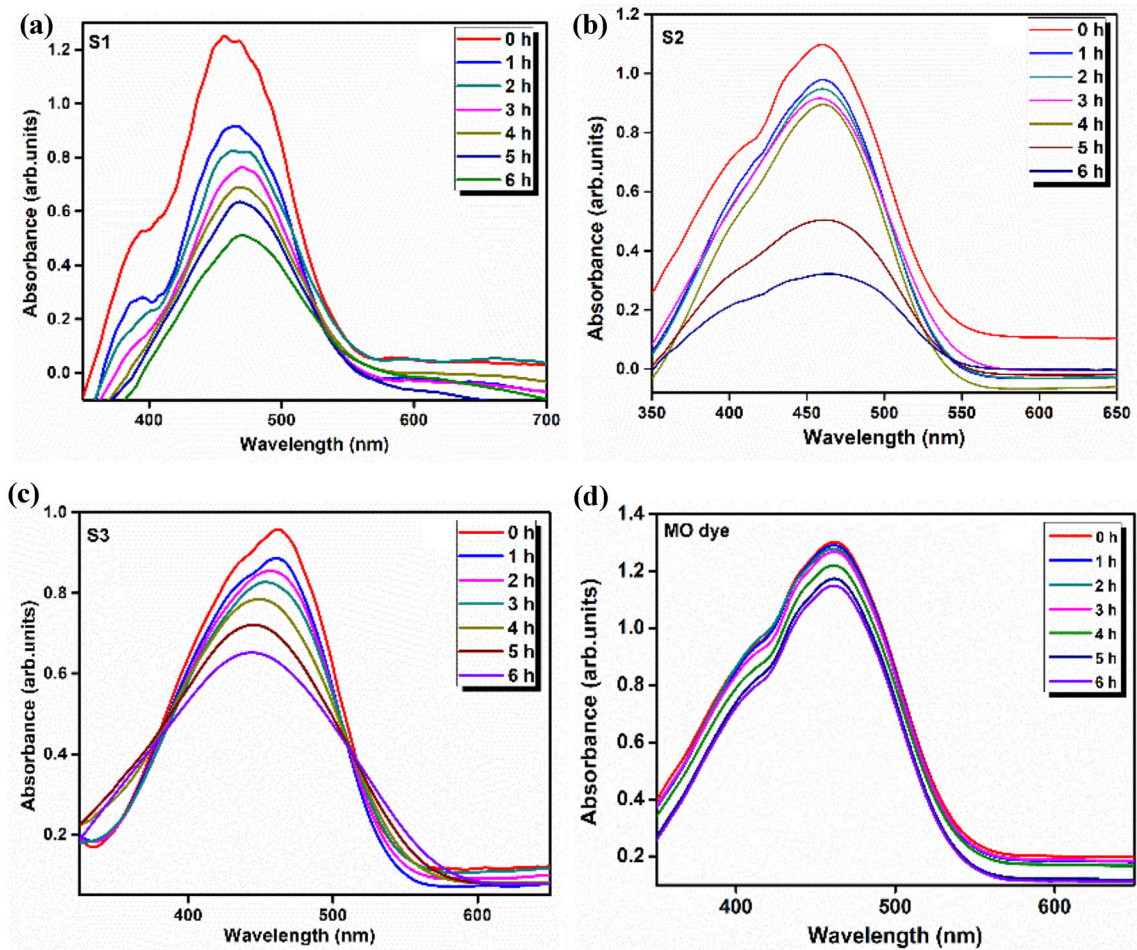
Fig. 11 Absorption spectra of MO dye solution in the presence of **a** S1, **b** S2, **c** S3 and **d** in absence of any catalyst
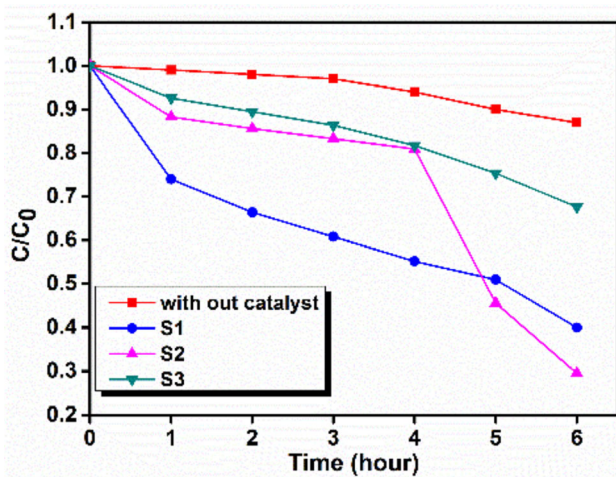

Fig. 12 Variation of degradation of MO dye solution in presence and absence of catalyst

the four kinds of kinetic models are presented in Fig. 13a – d, and the respective rate constants and

Table 3 MO dye degradation efficiency of all electrodeposited ZnO thin films

Sample name	Degradation efficiency (%)
MO dye	12.3
S1	60.0
S2	70.4
S3	32.3

linear correlation coefficients (R^2) are listed in Table 4. The table exhibits that, for all samples, the values of R^2 are close to unity for all four models, indicating that the photodegradation results of the synthesized thin films are pretty well explained by the zero-order, first-order, second-order, and modified Freundlich models. The modified Freundlich model actually suggests the adsorption of dye molecules on the surface of the catalysts. Moreover, the

Fig. 13 Photocatalytic degradation kinetic models: **a** Zero-order model, **b** first-order model, **c** second-order model, and **d** modified Freundlich model for electrodeposited ZnO thin films
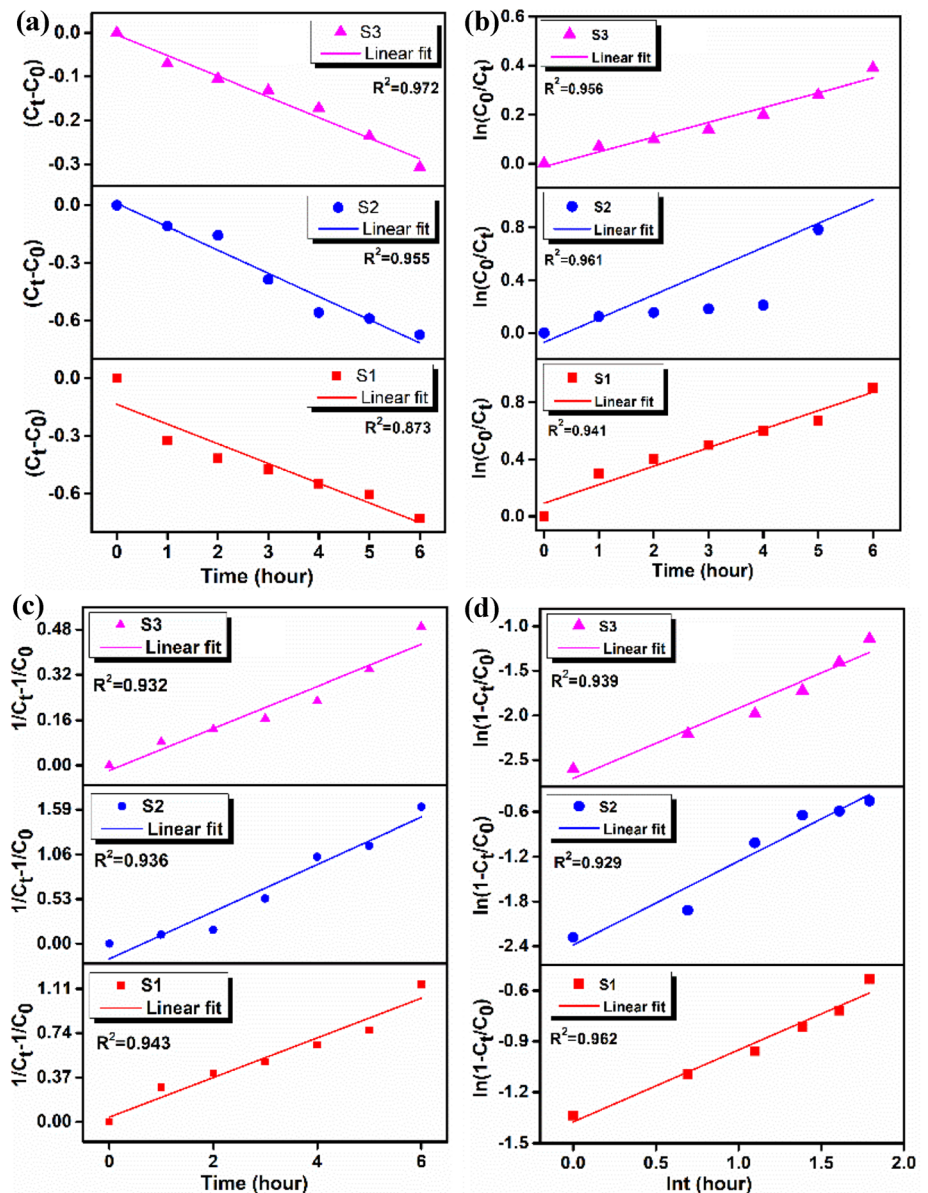

Table 4 R^2 and kinetic rate constants of photocatalytic degradation kinetic models applied to electrodeposited ZnO thin films

Photodegradation kinetic models	S1		S2		S3	
	R^2	K	R^2	K	R^2	K
Zero-order model	0.873	0.1027	0.955	0.1208	0.972	0.0470
First-order model	0.941	0.1310	0.961	0.1797	0.956	0.0603
Second-order model	0.943	0.1655	0.936	0.2804	0.932	0.0743
Modified Freundlich model	0.962	0.2520	0.929	0.092	0.939	0.066

zero-order, first-order, and second-order models refer to the removal of dye by photodegradation on the catalyst's surface. Therefore, the detailed analysis of the distribution of experimental data points in Fig. 13 reveals that the photocatalytic degradation of all the samples consists of mono linear models. Hence, the results declare that the removal of MO dye by using ZnO thin films is mainly controlled by: (a) adsorption–desorption of MO dye and (b) the

photocatalytic degradation of dye on the surface of the catalysts [57].

Furthermore, to get a better understanding about the photocatalytic performance of our system, the catalytic result of the present work is compared with the existing data of few similar works, which are listed in Table 5. The table exhibits that for the degradation of MO dye, a higher concentration of precursor has been used in the reported works. In contrast, our system achieved a decent photodegradation efficiency by using a very low precursor concentration. However, in our system, the irradiation time is high compared to the reported works because the amount of ZnO deposited on the substrate is lesser due to low precursor concentration. Hence, it indicates the presence of a low amount of catalyst during the photocatalytic experiments for our system and thus a higher irradiation time is required.

3.5.2 Photodegradation mechanism

Figure 14 exhibits the schematic diagram of the probable degradation mechanism of MO dye with ZnO thin films under UV light exposure. In the schematic, the positions of valance and conduction bands for ZnO (vs. vacuum) are considered as − 7.7 and − 4.4 eV, respectively [58].

In this mechanism, whenever ZnO thin films are irradiated with UV light, the electrons present on the V.B. of ZnO immediately get excited and goes into the C.B., leaving behind some holes in the V.B. The photogenerated electron–hole pairs move towards the catalyst's surface where different active sites are present to oxidize or reduce the electron acceptors or donors which eventually drive the catalytic reactions. At first, the holes oxidize the water molecules and
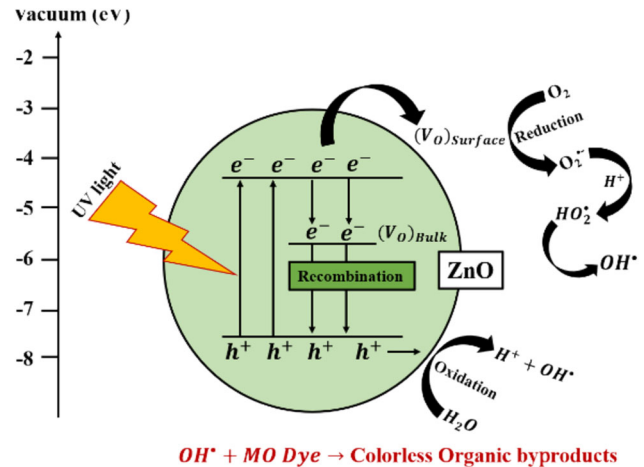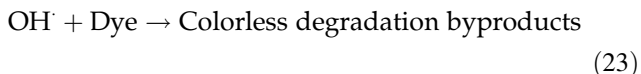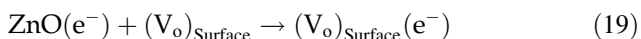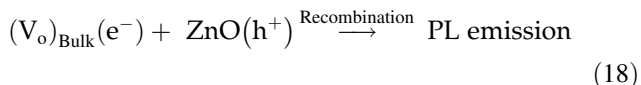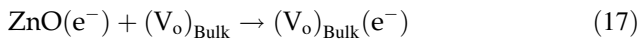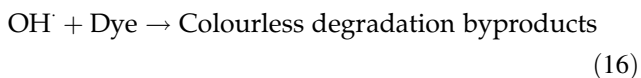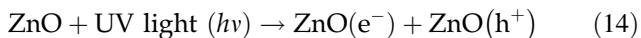

Fig. 14 Photocatalytic mechanism of electrodeposited ZnO thin films

create OH^- and H^+ ions. Subsequently, the MO dye molecules react with hydroxyl radicals and generate colorless degradation byproducts. On the other hand, the electrons are captured by the oxygen vacancy states present on the catalyst's surface and play an essential role as the carrier trapping centers. However, some bulk oxygen vacancies are also present in the ZnO lattice that can act as a recombination center and reduce photocatalytic activity. So, few electrons are trapped by these bulk oxygen vacancy states and electron–hole recombination occurs. By reducing oxygen molecules, the surface oxygen vacancy sites act as the active sites and produce oxygen radicals. These oxygen radicals then produce hydroxyl radicals after reacting with the hydrogen ions. Ultimately, the MO dye molecules react with these hydroxyl radicals and create colorless degradation byproducts. The complete reaction of the degradation mechanism

Table 5 Comparison of photocatalytic results of ZnO thin films with the existing literature

Catalyst	Precursor concentration (M)	Cationic Organic Dye	Light Source	Irradiation time (h)	Photocatalytic efficiency (%)	References
Electrodeposited ZnO thin films	0.075	MO	Sun light	3	≤ 50	[31]
ZnO thin films by hydrothermal method	0.01	MO	UV lamp (254 nm)	2	53.7	[32]
Electrodeposited ZnO thin films	0.01	MO	UV lamp (365 nm)	4	≤ 80	[33]
Electrodeposited ZnO thin films	0.002	MO	UV lamp (235 nm)	6	70.4	Present work

of MO dye in the presence of ZnO thin film is as follows

$$ZnO + UV\ light\ (h\nu) \rightarrow ZnO(e^-) + ZnO(h^+) \quad (14)$$

$$ZnO(h^+) + H_2O \rightarrow H^+ + OH^· \quad (15)$$

$$OH^· + Dye \rightarrow Colourless\ degradation\ byproducts \quad (16)$$

$$ZnO(e^-) + (V_o)_{Bulk} \rightarrow (V_o)_{Bulk}(e^-) \quad (17)$$

$$(V_o)_{Bulk}(e^-) + ZnO(h^+) \xrightarrow{Recombination} PL\ emission \quad (18)$$

$$ZnO(e^-) + (V_o)_{Surface} \rightarrow (V_o)_{Surface}(e^-) \quad (19)$$

$$(V_o)_{Surface}(e^-) + O_2 \rightarrow O_2^{·-} \quad (20)$$

$$O_2^{·-} + H^+ \rightarrow HO_2^· \quad (21)$$

$$2HO_2^· \rightarrow O_2^{·-} + H_2O_2 \rightarrow OH^- + OH^· + O_2 \quad (22)$$

$$OH^· + Dye \rightarrow Colorless\ degradation\ byproducts \quad (23)$$

The photocatalytic results of the ZnO thin films declare that the samples with nanosphere-like morphology (S1, S2) show better catalytic activity compared to the sample with a nanosheet-like structure (S3). However, various literature reported that the ZnO nanosheet always exhibits better photocatalytic performance than the ZnO nanosphere [59]. This is because the ZnO nanosheet has a large polar exposed surface (0001) compared to the nanosphere, which eventually helps to increase the surface oxygen vacancy concentration and hence shows a better catalytic performance. Actually, these surface vacancy states act as active sites and help in the redox reaction, which ultimately improves photocatalytic activity [60]. In our case, the green emission intensity of the PL spectra suggests that the ZnO nanosheet (S3) has a much higher surface oxygen vacancy concentration compared to the ZnO nanosphere (S1, S2). But, despite having a high surface oxygen vacancy concentration, the ZnO nanosheet has the lowest catalytic efficiency. On the other hand, the ZnO nanosphere has the highest catalytic efficiency despite the low surface oxygen vacancy concentration. This is because the surface oxygen vacancy concentration is too high in the case of the ZnO nanosheet (S3), and hence, a huge amount of bulk oxygen vacancies can easily be created. These bulk oxygen vacancies then play the role of recombination centers and finally reduce the photocatalytic

performance [61]. But, in the case of ZnO nanosphere samples, the photocatalytic efficiency is enhanced due to having an optimum concentration of the surface oxygen vacancy.

Again, the photocatalytic activity of each ZnO thin film (S1, S2, and S3) can also be elucidated by the variation of surface oxygen vacancy concentration. In general, the photocatalytic performance of any catalyst depends on many factors like crystallite size, surface area, the concentration of surface oxygen vacancy sites, etc. It is well known that the smaller the crystallite size of any catalyst higher will be the surface area. Hence, the availability of surface sites for the redox reaction increases, which eventually enhances the catalytic performance. However, the photocatalytic efficiency values of our ZnO thin films show an opposite trend (S2 > S1 > S3) compared to the order in which the catalytic performance should have changed with the crystallite size (S2 > S1 > S3). This implies that the catalytic performance of our samples can not be explained by the change of crystallite size or the variation of surface area. But, in the case of our thin films, the concentration of surface oxygen vacancy well illustrates the difference in the catalytic activities among all samples. The S1 sample shows less catalytic activity compared to S2 due to having a lower concentration of surface oxygen vacancy than S2. But, for the S3 sample, the presence of an excessive concentration of surface oxygen vacancy plays a negative role in the catalytic performance and reduces the catalytic efficiency. Hence, it is evident that due to having an optimum concentration of surface oxygen vacancy, the S2 sample exhibits the highest catalytic activity among the other thin film samples. The above discussion allows us to draw a significant conclusion that an optimum surface oxygen vacancy concentration can enhance the photocatalytic performance of any catalyst, while the surface oxygen vacancy can ruin the catalytic activity beyond that optimum level and reduce the photocatalytic performance.

4 Conclusions

With varying zinc nitrate concentrations in the electrolyte, a series of nanostructured ZnO thin films were synthesized in this work. The morphological evolution from 3D nanosphere-like structure to 2D nanosheet-like structure is observed for the

synthesized ZnO thin films with the increment of zinc nitrate concentration. The intensity variation of the ZnO-related diffraction peaks shows that the growth along the c-axis increases from S1 to S2, while it is further suppressed for S3. This variation in intensity establishes a correlation between the diffraction results and the nanostructures of the thin films. On the other hand, the ZnO-related diffraction peaks show a slight shifting ($-1°$) towards the higher 2θ angle, revealing the presence of micro-strain in all thin films. The estimated micro-strain values increase with increasing zinc nitrate concentration, which justifies the increment in crystal defects. The presence of Zn–O bond as well as the increment in the population of nitrate and –OH groups with increasing precursor concentration is confirmed for all thin films. The band edge absorption shows a redshift from the sample S1 to S2, indicating a reduction in bandgap and increment in crystallinity. In contrast, for the S3 sample, the band edge again exhibits a blue shift reflecting the increment in bandgap and decrease in crystallinity. For all the ZnO thin films, the enhancement in emission intensity with increasing precursor concentration is explained by the evolution of nanostructures, which can tune the defect states, and consequently luminescence is controlled. Finally, the photocatalytic results demonstrate the maximum degradation efficiency for S2 (70.43%), least for S3 (32.36%), and moderate for S1 (60%). The moderate degradation efficiency of S1 declares the presence of the lowest surface oxygen vacancy concentration compared to S2, while the huge surface oxygen vacancy is responsible for the lowest catalysis performance for the S3 sample. However, due to an optimum concentration of surface oxygen vacancy, the S2 sample shows the best photocatalytic efficiency. Therefore, we can conclude that, for the significant improvement in the photocatalytic activity of any catalyst, an optimum surface oxygen vacancy concentration is required, and beyond that optimum level, the catalytic performance gets diminished.

Acknowledgements

Declarations

Conflict of interest The authors declare that they have no conflicts to disclose.

References

1. C. Tian, Q. Zhang, A. Wu, M. Jiang, Z. Liang, B. Jiang, H. Fu, Chem. Commun. **48**(23), 2858–2860 (2012)
2. M. Gancheva, M. Markova-Velichkova, G. Atanasova, D. Kovacheva, I. Uzunov, R. Cukeva, Appl. Surf. Sci. **368**, 258–266 (2016)
3. L. Xu, Q. Chen, D. Xu, J. Phys. Chem. C **111**(31), 11560–11565 (2007)
4. İ Orak, Solid State Commun. **247**, 17–22 (2016)
5. H. Ohta, K.I. Kawamura, M. Orita, M. Hirano, N. Sarukura, H. Hosono, Appl. Phys. Lett. **77**(4), 475–477 (2000)
6. J.A. Rodriguez, T. Jirsak, J. Dvorak, S. Sambasivan, D. Fischer, J. Phys. Chem. B **104**(2), 319–328 (2000)
7. M. Rashad, N.M. Shaalan, A.M. Abd-Elnaiem, Desalin Water Treat. **57**(54), 26267–26273 (2016)
8. S.A. Taha, A.M. Abd-Elnaiem, M. Mohamed, S. Mostafa, M.S. Mostafa, Desalin Water Treat. **100**, 160–167 (2017)
9. M. Rashad, Opt. Quantum Electron. **51**(9), 1–13 (2019)
10. J. Han, F. Fan, C. Xu, S. Lin, M. Wei, X. Duan, Z.L. Wang, Nanotechnology **21**(40), 405203 (2010)
11. C.H. Xu, H.F. Lui, C. Surya, J. Electroceramics **28**(1), 27–33 (2012)
12. K. Sun, W. Wei, Y. Ding, Y. Jing, Z.L. Wang, D. Wang, Chem. Commun. **47**(27), 7776–7778 (2011)
13. A. Hongsingthong, I.A. Yunaz, S. Miyajima, M. Konagai, Sol. Energy Mater. Sol. Cells **95**(1), 171–174 (2011)
14. A.S. Riad, S.A. Mahmoud, A.A. Ibrahim, Phys. B Condens. Matter **296**(4), 319–325 (2001)
15. C. Ge, C. Xie, S. Cai, Mater. Sci. Eng. B **137**(1–3), 53–58 (2007)
16. S. Ilican, Y. Caglar, M. Caglar, J. Optoelectron. Adv. M. **10**(10), 2578–2583 (2008)
17. J.S. Wellings, N.B. Chaure, S.N. Heavens, I.M. Dharmadasa, Thin Solid Films **516**(12), 3893–3898 (2008)
18. F.F. Oliveira, M.P. Proenca, J.P. Araújo, J. Ventura, J. Mat. Sci. **51**(12), 5589–5597 (2016)
19. O. Lupan, T. Pauporté, L. Chow, B. Viana, F. Pellé, L.K. Ono, B.R. Cuenya, H. Heinrich, Appl. Surf. Sci. **256**(6), 1895–1907 (2010)
20. R. Liu, A.A. Vertegel, E.W. Bohannan, T.A. Sorenson, J.A. Switzer, Chem. Mater. **13**(2), 508–512 (2001)

21. N. Lehraki, A. Attaf, M.S. Aida, N. Attaf, M. Othmane, F. Bouaichi, arXiv **2003**, 08487 (2020)

22. S. Saravanan, R.S. Dubey, AIP Conf. Proc. **2117**, 020001 (2019)

23. A.S. Hamidi, M.S.Z. Abidin, Electrochemical deposition of Zinc Oxide thin film using two-terminal setup. 2017 IEEE Regional Symposium on Micro and Nanoelectronics (RSM). IEEE, 2017

24. J. Yang, Y. Wang, J. Kong, H. Jia, Z. Wang, Opt. Mat. **46**, 179–185 (2015)

25. K. Dakhsi, R. Belkhamina, M.E. Touhami, Z. El Khalidi, B. Hartiti, A. Ridah, P. Thevenin, Effect study of precursor concentration of ZnO crystals obtained by electrode position. 2015 3rd International Renewable and Sustainable Energy Conference (IRSEC). IEEE, 2015

26. T. Singh, D.K. Pandya, R. Singh, Appl. Surf. Sci. **270**, 578–583 (2013)

27. B. Xue, Y. Liang, L. Donglai, N. Eryong, S. Congli, F. Huanhuan, S. Xiaosong, Appl. Surf. Sci **257**(24), 10317–10321 (2011)

28. D. Pradhan, K.T. Leung, Langmuir **24**(17), 9707–9716 (2008)

29. M.R. Khajavi, D.J. Blackwood, G. Cabanero, R. Tena-Zaera, Electrochim. Acta **69**, 181–189 (2012)

30. G. Yao, M. Zhang, J. Lv, K. Xu, S. Shi, Z. Gong, J. Tao, X. Jiang, L. Yang, Y. Cheng, G. He, J. Electrochem. Soc **162**(7), D300 (2015)

31. M. Zhao, Y. Cheng, J. Lv, Y. Zhang, W. Zhu, G. He, Z. Sun, J. Mater. Sci. Mater. Electron. **28**(3), 2731–2738 (2017)

32. J. Lv, F. Shang, G. Pan, F. Wang, Z. Zhou, C. Liu, F. Liu, J. Mater. Sci. Mater. Electron. **25**(2), 882–887 (2014)

33. F.A. Cataño, H. Gomez, E.A. Dalchiele, R.E. Marotti, Int. J. Electrochem. Sci. **9**, 534–548 (2014)

34. C. Wang, D. Wu, P. Wang, Y. Ao, J. Hou, J. Qian, Appl. Surf. Sci. **325**, 112–116 (2015)

35. J. Lv, W. Gong, K. Huang, J. Zhu, F. Meng, X. Song, Z. Sun, Superlattice Microst. **50**(2), 98–106 (2011)

36. L. Yang, Z.H. Kang, Z.H. Chen, I. Shafiq, J.A. Zapien, I. Bello, W.J. Zhang, S.T. Lee, Cryst. Growth Des. **9**(7), 3222–3227 (2009)

37. J. Zhang, L. Sun, J. Yin, H. Su, C. Liao, C. Yan, Chem. Mater. **14**, 4172–4177 (2002)

38. D. Banerjee, A.K. Kar, J. Alloys Compd. **859**, 157793 (2021)

39. P. Basnet, D. Samanta, T.I. Chanu, J. Mukherjee, S. Chatterjee, SN Appl. Sci. **1**(6), 633 (2019)

40. G.S. Thool, A.K. Singh, R.S. Singh, A. Gupta, M.A.B.H. Susan, J. Saudi Chem. Soc. **18**(5), 712–721 (2014)

41. V. Biju, N. Sugathan, V. Vrinda, S.L. Salini, J. Mater. Sci. **43**(4), 1175–1179 (2008)

42. D. Wu, Y. Jiang, J. Liu, Y. Yuan, J. Wu, K. Jiang, D. Xue, Nanoscale Res. Lett. **5**(11), 1779 (2010)

43. G.N. Dar, A. Umar, S.A. Zaidi, A.A. Ibrahim, M. Abaker, S. Baskoutas, M.S. Al-Assiri, Sens. Actuators B **173**, 72–78 (2012)

44. M.S. Chauhan, R. Kumar, A. Umar, S. Chauhan, G. Kumar, M. Faisal, A. Al-Hajry, J. Nanosci. Nanotechnol. **11**(5), 4061–4066 (2011)

45. O. Yayapao, T. Thongtem, A. Phuruangrat, S. Thongtem, Mater. Lett. **90**, 83–86 (2013)

46. K. Singh, D.K. Shukla, S. Majid, R. Dhar, R.J. Choudhary, D.M. Phase, J. Phys. Conf. Ser. **755**(1), 012040 (2016)

47. H.E. Redmond, K.D. Dial, J.E. Thompson, Aeolian Res. **2**(1), 5–26 (2010)

48. M.Y. Ali, M.K.R. Khan, A.T. Karim, M.M. Rahman, M. Kamruzzaman, Heliyon **6**(3), e03588 (2020)

49. G. Patwari, P.K. Kalita, R. Singha, Mater. Sci. Poland **34**(1), 69–78 (2016)

50. M.M.H. Farooqi, R.K. Srivastava, Effect of Annealing Temperature on Structural, Photoluminescence and Photoconductivity Properties of ZnO Thin Film Deposited on Glass Substrate by Sol–Gel Spin Coating Method. Proc. Natl. Acad. Sci. India Sect. A Phys. Sci. (2019)

51. D. Banerjee, A.K. Kar, Opt. Mater. **89**, 430–440 (2019)

52. M. Fu, Y. Li, P. Lu, J. Liu, F. Dong, Appl. Surf. Sci. **258**(4), 1587–1591 (2011)

53. M.J. Uddin, M.M. Alam, M.A. Islam, S.R. Snigda, S. Das, M.M. Rahman, M.N. Uddin, C.A. Morris, R.D. Gonzalez, U. Diebold, T.J. Dickens, Int. Nano Lett. **3**(1), 1–10 (2013)

54. P. Sharma, N. Kumar, R. Chauhan, V. Singh, V.C. Srivastava, R. Bhatnagar, Chem. Eng. J. **392**, 123746 (2020)

55. S. Talebi, N. Chaibakhsh, Z. Moradi-Shoeili, J. Appl. Res. Technol. **15**(4), 378–385 (2017)

56. J.H. Yang, Y.S. Han, M. Park, T. Park, S.J. Hwang, J.H. Choy, Chem. Mater. **19**(10), 2679–2685 (2007)

57. Y.A.N.G. Qingshan, L.I.A.O. Yongjin, M.A.O. Lingling, Chin. J. Chem. Eng. **20**(3), 572–576 (2012)

58. A. Hagfeldt, M. Graetzel, Chem. Rev. **95**(1), 49–68 (1995)

59. R. Singh, K. Verma, A. Patyal, I. Sharma, P.B. Barman, D. Sharma, Solid State Sci. **89**, 1–14 (2019)

60. C. Wang, D. Wu, P. Wang, Y. Ao, J. Hou, J. Qian, App. Surf. Sci. **325**, 112–116 (2015)

61. J. Hu, N. You, Z. Yu, G. Zhou, X.J. Xu, J. Appl. Phys. **120**(7), 074301 (2016)